

Thermoreflectance-based approach for surface temperature measurements of thin-film gold sensors ^{EP}

Cite as: Rev. Sci. Instrum. **94**, 034902 (2023); <https://doi.org/10.1063/5.0129312>

Submitted: 04 October 2022 • Accepted: 17 February 2023 • Published Online: 13 March 2023

 L. Farbaniec and  D. E. Eakins

COLLECTIONS

 This paper was selected as an Editor's Pick



View Online



Export Citation



CrossMark

ARTICLES YOU MAY BE INTERESTED IN

[Spatial heterodyne spectroscopy for fast local magnetic field measurements of magnetized fusion plasmas](#)

Review of Scientific Instruments **94**, 033504 (2023); <https://doi.org/10.1063/5.0127165>

[Infrared compatible rapid mixer to probe millisecond chemical kinetics](#)

Review of Scientific Instruments **94**, 034102 (2023); <https://doi.org/10.1063/5.0121817>

[A new high parallel-field spectrometer at TRIUMF's \$\beta\$ -NMR facility](#)

Review of Scientific Instruments **94**, 023305 (2023); <https://doi.org/10.1063/5.0137368>



Time to get excited.

Lock-in Amplifiers – from DC to 8.5 GHz



[Find out more](#)
 Zurich Instruments

Thermoreflectance-based approach for surface temperature measurements of thin-film gold sensors

Cite as: Rev. Sci. Instrum. 94, 034902 (2023); doi: 10.1063/5.0129312

Submitted: 4 October 2022 • Accepted: 17 February 2023 •

Published Online: 13 March 2023



L. Farbaniec^{1,2,3,a)}  and D. E. Eakins^{1,2} 

AFFILIATIONS

¹ Institute of Shock Physics, Imperial College London, London SW7 2AZ, United Kingdom

² Department of Engineering Science, University of Oxford, Parks Road, Oxford OX1 3PJ, United Kingdom

³ Faculty of Physics and Applied Computer Science, AGH University of Science and Technology, Al. Mickiewicza 30, 30-059 Kraków, Poland

^{a)} Author to whom correspondence should be addressed: lukasz.farbaniec@eng.ox.ac.uk

ABSTRACT

A novel thermoreflectance-based diagnostic tool capable of visualizing spatial and temporal changes in surface temperature is presented. The method uses narrow spectral emission bands of blue [$\lambda = 405$ nm with 10 nm full-width-at-half-maximum (FWHM)] and green ($\lambda = 532$ nm with 10 nm FWHM) light to monitor the optical properties of gold and thin-film gold sensors, relating changes in reflectivity to temperature through a known calibration coefficient. The system is made robust to tilt and surface roughness variations through the simultaneous measurement of both probing channels with a single camera. Experimental validation is performed on two forms of gold materials heated from room temperature to 200 °C at a rate of ~100 °C/min. Subsequent image analysis shows perceptible changes in reflectivity in the narrow band of green light, while the blue light remains temperature-insensitive. The reflectivity measurements are used to calibrate a predictive model with temperature-dependent parameters. The physical interpretation of the modeling results is given, and the strengths and limitations of the presented approach are discussed.

Published under an exclusive license by AIP Publishing. <https://doi.org/10.1063/5.0129312>

I. INTRODUCTION

Temperature is a fundamental condition needed to help define the thermodynamic state of a material. As such, the measurement of such fields finds importance throughout a wide range of activities, including scientific research, technology development, and industry, where imaging of non-uniform thermal fields is desired. For example, the analysis of transient thermal effects in electronic systems under operating conditions is critical in their validation process. In the manufacturing sector, thermal imaging is used to monitor the condition of the equipment in order to identify and avoid problems with its failure in advance. Another example here would be the automotive industry, which uses thermography-based approaches to study the thermal behavior during load tests of fast-rotating stressed parts, such as brake discs. In materials research, knowledge of the material's thermal history helps to shed light on the mechanisms responsible for micro-/meso-scale stress relaxation culminating in

damage at the bulk scale. These and many other applications require accurate, fine spatial scale and often non-contact measurements of temperature.

In general, there are two main approaches to thermal imaging. The first estimates the temperature based on the radiation passively emitted by an object according to Planck's law, and is represented by the class of techniques known as "pyrometry."^{1,2} The other one, known as "thermoreflectance," relies upon the change in intensity of light reflected by the object.^{3–5} In view of the aforementioned applications, pyrometry-based techniques must contend with several key challenges. In particular, temperature measurements of reflective materials and shiny metals are troublesome, considering the fact that they are inefficient emitters and radiate very little thermal energy. As a matter of fact, the measured signals of highly reflective surfaces can be easily dominated by the background "radiators" with higher emissivity. Furthermore, different materials such as glass, plastics, and metals have different emissivity.

Thus, the objects of different material types emit unequal radiation even if they experience the same temperatures. These can make the infrared measurements uncertain if the emissivity of visualized objects is not known. Also, given the fact that different materials have different peak energies and most infrared devices can cover only a narrow wavelength range to which they are sensitive, there is no universal device or approach that fits all applications. The thermoreflectance method also comes with its own limitations. The most important is that the changes in reflectance associated with typical temperature shifts (a few tens–hundreds of degrees) are small and difficult to quantify for most of the materials. Also, the observed changes in reflectance can be easily misinterpreted when the object is in motion or tilts away from the light source. The technique does have some distinct advantages over pyrometry, however, most notably the shift from the detection of passive radiation to active illumination. While signal-to-noise in pyrometry measurements is ultimately related to the temperature of the specimen, which furthermore places practical restrictions on integration times, the signals for thermoreflectance can be made arbitrarily strong using ultra-bright illumination sources, enabling relatively “fast” gating at even modest temperatures.

The existing thermoreflectance approaches are based on either time or frequency domain imaging. In time domain thermoreflectance imaging, the light reflected from an object is collected by the camera sensor as a function of time. The collected signal is then compared with the reference signal (“cold” frame) to measure the relative change in light intensity. Since there is a linear relationship between reflectivity and surface temperature, the thermoreflectance coefficient can be quantified, and the measured reflectivity change is converted to the change in temperature. This approach has been successfully applied for high-resolution surface temperature mapping of various micro-/nanoscale devices.^{6–11} The frequency domain approach is measuring the temperature based on the response of a sample to periodic temperature oscillations.^{12–16} The thermal properties are obtained by minimizing the difference between the measured and calculated phase lag at the stimulation frequencies by adjusting the parameters of a thermal model. Although these two thermoreflectance approaches are equivalent, the time domain approach is physically more intuitive and often favored when it comes to scenarios where externally applied heat pulses are not possible, such as in the case of dynamic mechanical processes where strain evolves faster than thermal conduction (adiabatic condition).

In this study, a novel time domain thermoreflectance method is presented for conducting measurements of surface temperature fields at high speed. Whereas previous high speed thermoreflectance techniques relied upon spectrally resolving reflected light at the expense of spatial resolution, the current approach provides for high spatial resolution through the application of precalibrated reflectance properties. Furthermore, the current technique minimizes errors caused by tilt/roughness and camera electronics through the simultaneous recording of two probing channels with a single monochromatic high-speed camera. The experiments are conducted on gold, as the reflectivity of this metal varies significantly with temperature across readily accessible illumination wavelengths.^{17–21} The second reason for selecting this material is its potential use as a thin-film temperature sensor that can be applied to other material systems to measure their temperature with greater

accuracy. This can be compared to the approach adopted in the infrared technology, where high-emissivity tapes or paints are used on a low-emissivity target. Here, however, we are using the current state of technology development in lighting, optics, and high-speed imaging systems allowing for spatial and temporal measurements of temperature not accessible to commercially available systems at the moment. We also review the theory and practical aspects of thermoreflectance measurements in relation to the proposed methodology, and present predictive modeling for the reflectivity changes of gold in different thermal states.

II. THERMOREFLECTANCE ANALYSIS

The proposed method relies upon the principle of thermoreflectance, where one can observe the change in reflectivity of a material due to exposure to different temperatures. For different wavelengths, these changes may be gradual or rapid and can reflect positive, negative, or no change from the previous state. Thus, if the reflectance of a surface (R) is defined as the ratio between the intensity of light reflected from a surface (I_R) and the intensity of incident light (I_I), the change in reflectance (ΔR) between two distinct times ($t_{i=0,1}$) can be expressed as follows:

$$\Delta R(\lambda_i, t_1) = R(\lambda_i, t_1) - R(\lambda_i, t_0), \quad (1)$$

where the illumination intensity at wavelength λ_i is regarded as constant over this time.

Consequently, the relation between the relative change in reflectivity and the temperature change ($\Delta \mathcal{T}$) between two distinct times can be expressed in terms of the thermoreflectance coefficient (κ) as follows:

$$\frac{\Delta R(\lambda_i, t_1)}{R(\lambda_i, t_0)} = \frac{I_R(\lambda_i, t_1)}{I_R(\lambda_i, t_0)} - 1 = \kappa_i \Delta \mathcal{T}(t_1). \quad (2)$$

The value of κ_i is unique for each material (surface characteristics, chemical composition, etc.), and illumination wavelength, and must be known *a priori* to relate reflectivity to temperature. The temperature at the reference time t_0 should also be known and determined in advance.

Next, consider the case where the target surface orientation and/or roughness has changed. In that case, the reflected light is modulated by a factor A , i.e.,

$$I_R^*(\lambda_i, t_2) = A(\alpha, \rho, \dots) I_R(\lambda_i, t_1), \quad (3)$$

where the asterisk is used to indicate the measurement in the new configuration at time t_2 , and A is shown to depend upon physical characteristics such as tilt (α) and roughness (ρ). Thus, the determination of temperature in this manner requires the instantaneous modulation factor to be known. As this would require real-time characterization of the physical characteristics of the surface, an alternative approach is to introduce a second measurement wavelength, where it is assumed that the effect of tilt and/or roughness affects all wavelengths equally. This argument also requires certain assumptions like the random structure of surface roughness, to avoid introducing wavelength-dependent concepts of diffuse reflectivity or interference effects. The temperature can, therefore, be determined through real-time measurements of reflected

intensity at two wavelengths, along with known coefficients of thermorefectance at these two wavelengths as follows:

$$\Delta\mathcal{T}(t) = \frac{I_R^*(\lambda_1, t) I_R(\lambda_2, t_0) - I_R^*(\lambda_2, t) I_R(\lambda_1, t_0)}{\kappa_2 I_R^*(\lambda_1, t) I_R(\lambda_2, t_0) - \kappa_1 I_R^*(\lambda_2, t) I_R(\lambda_1, t_0)}. \quad (4)$$

In the case of gold, we can choose these wavelengths out of convenience to minimize uncertainty in temperature. For instance, κ of gold over the range of 400–420 nm is very small ($\sim 1 \times 10^{-5} \text{ K}^{-1}$),^{12,19} and, thus, there is no perceptible change in reflectivity across the spectral emission band of blue light for modest temperature excursions. The corresponding change in reflectivity is less than 1% up to 500 °C.²² Selecting a second wavelength at 532 nm, which exhibits a relatively strong response to temperature, the change in temperature can be determined through the following simplified expression:

$$\Delta\mathcal{T}(t_i) = \frac{1}{\kappa_g} \left(\frac{I_R(\lambda_b, t_0) I_R^*(\lambda_g, t_i)}{I_R^*(\lambda_b, t_i) I_R(\lambda_g, t_0)} - 1 \right), \quad (5)$$

where the λ_b and λ_g symbols are used to indicate the measurements at wavelengths of 405 and 532 nm, respectively.

Consequently, the temperature of a gold film undergoing both heating/cooling and surface modification can be determined through simultaneous measurement of the relative reflected intensity at these two wavelengths.

III. EXPERIMENTAL SETUP

A. Optical components

Figure 1(a) shows the experimental configuration developed for these high-speed thermorefectance imaging measurements. A single optical breadboard supports a light source and an array of optical components mounted in a 60 mm cage system. The path that light rays travel from the light source to the camera is as follows: First, a mixed beam of light of two single color LEDs (hereafter, referred to as the “green” and “blue” channels) is directed to a non-polarizing beamsplitter cube (50:50 R:T ratio). The reflected light is directed toward the specimen, and the other half is transmitted through it, enabling “on-shot” measurement of illumination

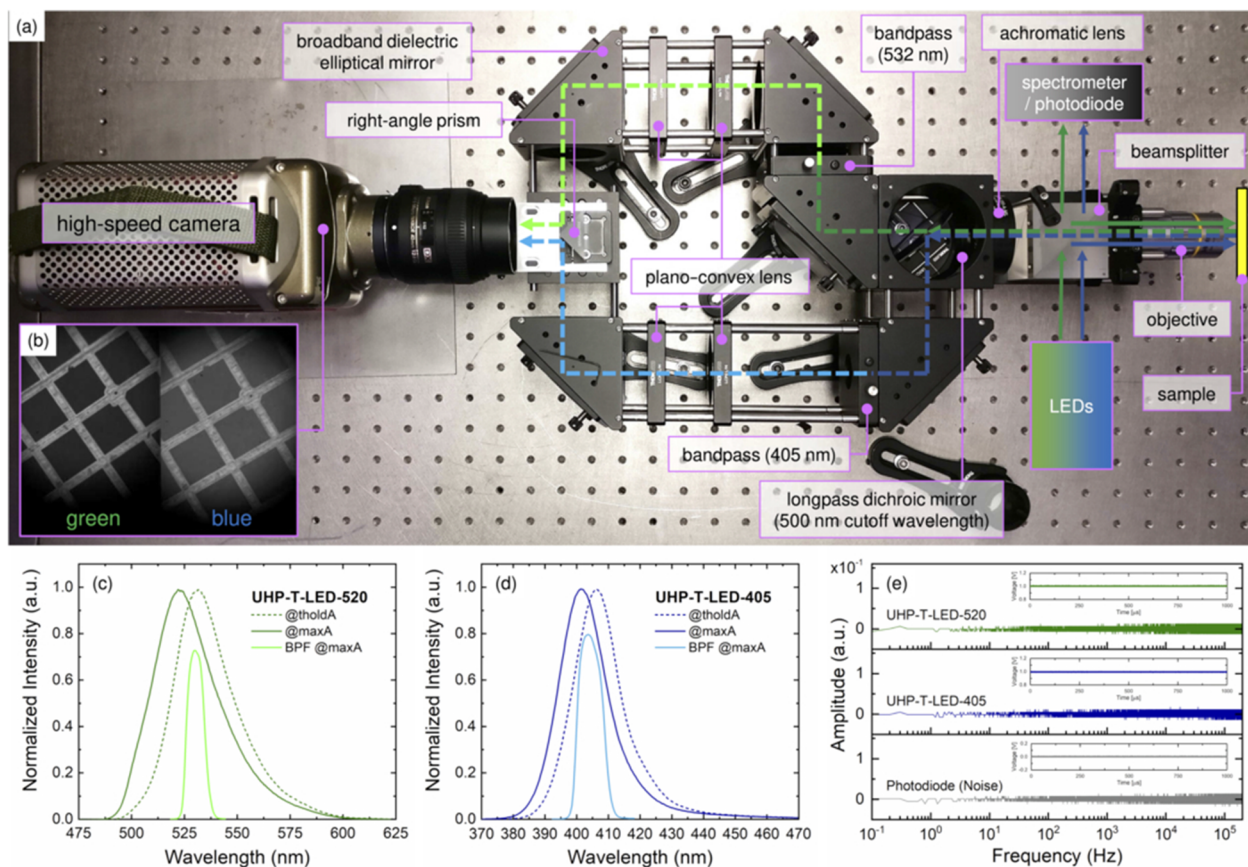


FIG. 1. (a) Experimental platform for thermorefectance imaging; (b) image formed on the sensor of the camera showing the object illuminated by the green (left side image) and blue (right side image) LEDs; (c) normalized emission spectrum as a function of the wavelength for the green LED; (d) normalized emission spectrum as a function of the wavelength for the blue LED; and (e) power spectra resulting from the output voltage signals acquired by the detector (the insets of subfigures show the acquired 1 ms long signals).

characteristics using a spectrometer/photodiode. The reflected light passes through the center of a microscope objective (10× Plan Apo long working distance objective), which acts as both an imaging system and a condenser and forms a diffraction-limited spot on the surface of the sample. It should be noted that this objective can be substituted for any other apochromatic objective to obtain the desired field of view/magnification. The light is then reflected off the specimen back through the objective and the beamsplitter. Due to the second pass through the beamsplitter, 50% of the reflected light from the specimen is redirected away from the principle direction of travel. The remaining light propagates further through an achromatic doublet lens ($f = 150$ mm) and arrives at a longpass dichroic mirror (505 nm cutoff wavelength) at a 45° angle of incidence. At this location, the light is separated into two single-color rays such that the “green” rays propagate through the longpass dichroic mirror, and the “blue” rays are reflected from it by 90° . Consequently, the separated rays are directed by a series of broadband dielectric elliptical mirrors to a knife-edge right-angle prism mirror, where the rays meet again and propagate parallel to each other with a small offset. On the path between the longpass dichroic mirror and the prism mirror, the rays pass through a bandpass filter [central wavelength (CWL) 405 ± 2 nm, full-width-at-half-maximum (FWHM) 10 ± 2 nm in the “blue” channel, and CWL 532 ± 2 nm, FWHM 10 ± 2 nm in the “green” channel] and two plano-convex lenses ($f = 150$ mm). The bandpass filters narrow the bandwidth of the collected light to the range of interest, while the lenses are used to establish an image plane at the edge of the right-angle prism. The distance between the specimen and the prism mirror is the same for both color channels. Thus, both channels reconstruct an image with the same magnification at the focal point. The image is then relayed to the sensor of a camera (Phantom v7.3) with a Nikon (40 mm f/2.8) lens. As a result, the collected image [Fig. 1(b)] is composed of two images showing the same object illuminated by narrow-band green (left side image) and blue lights (right side image), respectively. Finally, it should be emphasized that reflectance thermometry is an active probing technique, which allows us to adjust the illumination power of LEDs to attain a sufficient signal-to-noise ratio for the desired exposure time.

The last step of this approach is concerned with image analysis. The acquired images need to be processed such that the correspondence of a single pixel (or small neighborhood around the pixel of interest) in one image can be found in the following images. This requires a pixel-to-pixel correlation between the images and also matching pixels from two imaging channels on the same image. This can be accomplished by the implementation of digital-image-correlation (DIC) algorithms. As a result, a dataset where each pixel contains information on the intensity of blue and green lights reflected from a discrete area of the specimen is obtained. Measured over time, such an approach enables the reflectance change for each pixel and ultimately the 2D temperature field to be monitored. Finally, it is worth mentioning that such data analysis expects the experiments to be conducted with a single camera since the data acquisition with two separate cameras might introduce errors in the spatial correlation between images captured at slightly different times.²³

B. Illumination source

High-speed photography and related dynamic imaging methods require substantial radiant power to capture images with high

contrast and signal-to-noise within short exposure times. A good light source, in the context of time-resolved dynamic reflectance measurements, should not only have high brightness with spectral emission in the wavelength range of interest but also high levels of stability and repeatability of output intensity. These factors are essential for reflectance measurements that require sequential data acquisitions with sampling rates up to several MHz. Although there are many high-power light source technologies available on the market, their potential use in such measurements is limited. For example, xenon-based flash lamps can provide reasonable amounts of light across the visible spectrum but suffer from temporal variations in power output. Laser-based illumination, on the other hand, can provide high energy and long-term output power stability at discrete wavelengths but suffers from so-called “speckle” intensity modulations originating from the spatially coherent nature of the laser beam. In this study, single-chip and single-color ultra-high brightness LEDs that produce narrow spectral emission bands of light were chosen because they provide the best compromise between spatial and temporal measurements of reflectance with discrete wavelength bands.

Figures 1(c) and 1(d) show a normalized emission spectrum as a function of wavelength for the LEDs used in this study. It should be noted that one characteristic of the LED technology is that the emitted spectrum can be shifted by changing the LED drive current. The shift of the central wavelength of the emission spectrum is, however, difficult to quantify since the temperature of the operating LED system is another factor to consider. In the case of the “green” LED (Prizmatix UHP-T-LED-520), the central wavelength of the LED shifts from 532 to 523 nm by adjusting the power between the threshold and maximum levels. The spectral width of the source (full-width-at-half-maximum) is ~ 36 nm, and the collimated optical power output is up to 1.2 W. The central wavelength of the emitted light from the “blue” LED (Prizmatix UHP-T-LED-405) can shift from 406 to 402 nm by varying the power from the threshold to the maximum value. The spectral width of this light source is ~ 19 nm, and the collimated optical power output is up to 3.8 W. The changes in emission spectral shape can be, however, ignored since the narrow bandpass filters are used in the experimental platform that limit the bandwidth of the output signal to the band allocated for thermorefectance measurements. Each bandpass filter provides high transmission in specified wavelength regions (at least 85% for central wavelengths of bandpass filters), and these are also shown in Figs. 1(c) and 1(d). Thus, in such a configuration, the errors in the measurement might occur in two scenarios: (i) when the LEDs are driven at different illumination intensity levels prior to (when exploring the temperature-dependent optical properties of the test specimens) and during the tests and (ii) when voltage or current fluctuations are present in the circuit to which the LEDs are connected. One can, therefore, minimize these effects by using a stable power source with a precise adjustment range of target parameters, conducting all measurements at the same operating current, or correcting them by real-time measurements of the emitted light beams (e.g., by taking the transmitted light through the first beamsplitter, as shown in Fig. 1).

Here, a quantitative analysis of intensity fluctuations in the emitted light from stabilized LEDs was performed by evaluating the intensity of light incident on the photodiode (Thorlabs DET10A/M) prior to the thermorefectance measurement. Figure 1(e) shows the

power spectrum results, which are based on the output voltage signals acquired by the detector for 10 s at a sampling rate of 200 kHz. Note that none of the voltage signals (1 ms long signal sequences are shown in the insets of subfigures) is contaminated with drift or visually evident periodic components. As a matter of fact, the potential voltage fluctuations caused by the emitted light from the LEDs are within the range of the background noise level in an electronic system (combined vertical noise of the oscilloscope and the photodiode) and have comparable rms amplitudes of voltage fluctuations. Thus, it is expected to see the power spectrum of the signal constant over all the frequencies. This, in turn, suggests a stable and constant light emission from the LEDs over a wide range of temporal scales.

IV. EXPERIMENTAL VALIDATION

A. Flat mirror tilt

In Sec. II, the modulation factor (A) has been introduced and used as a parameter reflecting changes in the target surface orientation and/or roughness. To ensure that this factor is arising from athermal changes to surface properties and is equally present in both color channels, a validation experiment illustrating this principle has been conducted, as shown in Figs. 2(a)–2(d). A broadband dielectric mirror was placed in front of the experimental platform and tilted such that the angle of incidence changed by $\pm 5^\circ$ [Fig. 2(a)]. As the mirror tilts away from the normal axis, the amount of light collected by the objective lens drops rapidly. This can be seen in the photographs taken during the experiment [Fig. 2(b)]. Note the nonuniform intensity distribution of light with a gradual reduction of image brightness in the peripheral regions of both imaging channels. Figure 2(c) helps to show this result through the two-dimensional representation of the intensities of pixels along a line within the image, where the x -axis represents the horizontal distance through the image and the y -axis represents the vertically averaged pixel intensity, as shown in Fig. 2(b). The peak intensity values corresponding to both color channels were then used to calculate the change in reflectance, ΔR , normalized to the 0° case, in which the light was incident close to normal [Fig. 2(d)]. Note that the reflectance ratio is the same for both color channels, which indicates a good alignment of the system components, and more importantly, supports the assumption that the athermal changes in surface properties affect both channels equally.

B. Gold film

As discussed earlier, changes in reflectivity across the spectral emission band of blue light are only related to the specimen's tilt and surface changes. The changes in reflectivity across the spectral emission band of green light, in addition to sensitivity to the specimen's tilt and surface changes, are also associated with the changes in temperature. Figures 3(a)–3(d) show a validation experiment illustrating the sensitivity of reflectance to the temporal variation in the temperature of a thin layer of gold. The gold film was deposited on a sapphire window, placed on a heating stage, and heated up to high temperatures (from room temperature to 200°C in ~ 2 min). The surface temperature was measured by two thermocouples located near the imaged area, as shown in Fig. 3(a). A photograph taken during the experiment is shown in Fig. 3(b). The camera was set up to record video at a resolution of 640×480 pixels, at a frame rate of 10 fps, and a single exposure time of $10\ \mu\text{s}$. In this case, the term “dynamic measurement” refers only to the short exposure time since the used high-speed camera trades off spatial resolution for temporal resolution. Also indicated in Fig. 3(b) are the regions used to calculate the average light intensity collected by the camera during the experiment [shown in Fig. 3(c)]. Note that the reflectance change (drop in the light intensity) with the progression of time was observed for the green color channel, while the blue color channel maintained near constant light intensity during the whole experiment. Subsequently, the resulting reflectivity change as a function of measured temperature is shown in Fig. 3(d).

C. Gold grid

One of the main characteristics of this method is the spatial reflectance measurements, as shown in Figs. 4(a)–4(e). In this experiment, a gold grid sample was placed on a heating stage and, subsequently, heated up to 200°C in ~ 2 min. A schematic diagram of the experimental setup is shown in Fig. 4(a), while the area of the specimen visualized during the test is shown in Fig. 4(b). The photographs were taken at a frame rate of 10 fps, a single exposure time of $10\ \mu\text{s}$, and a resolution of 640×480 pixels. The average light intensity collected by the camera during the experiment was calculated within the area of the whole sample. As in the previous case, the increase in temperature caused the reduction of pixel intensity for the green color channel, and the blue color channel remained temperature insensitive [Fig. 4(c)]. However, because the

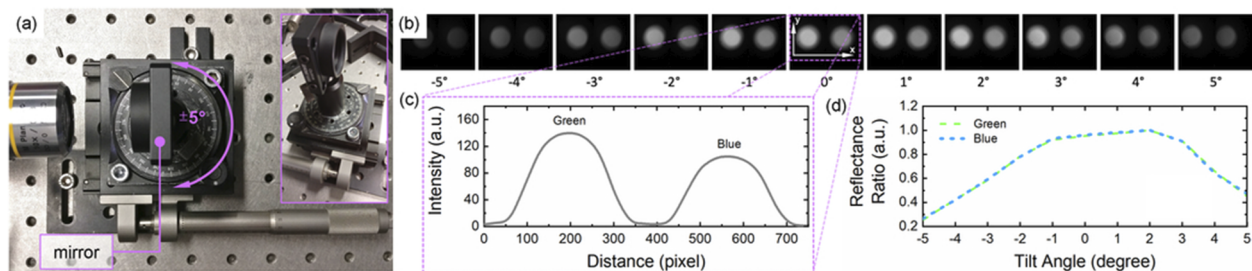


FIG. 2. (a) Validation experiment illustrating the robustness of the system against the tilt of the optical axis; (b) mirror reflection photographs for the angle of incidence $\pm 5^\circ$; (c) two-dimensional representation of the intensities of pixels along a line within the image, where the x -axis represents the horizontal distance through the image and the y -axis the vertically averaged pixel intensity; and (d) change in reflectance, ΔR , normalized to the 0° case.

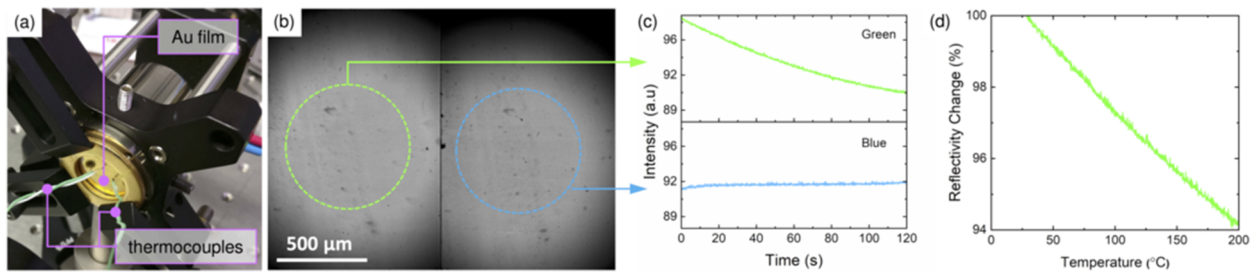


FIG. 3. (a) Validation experiment illustrating the sensitivity of reflectance to the temporal variation in the temperature; (b) photograph of the gold film with highlighted regions used for the average pixel intensity calculations; (c) average pixel intensities in the area of interest in each color channel plotted with respect to time; and (d) reflectivity change as a function of temperature measured with thermocouples.

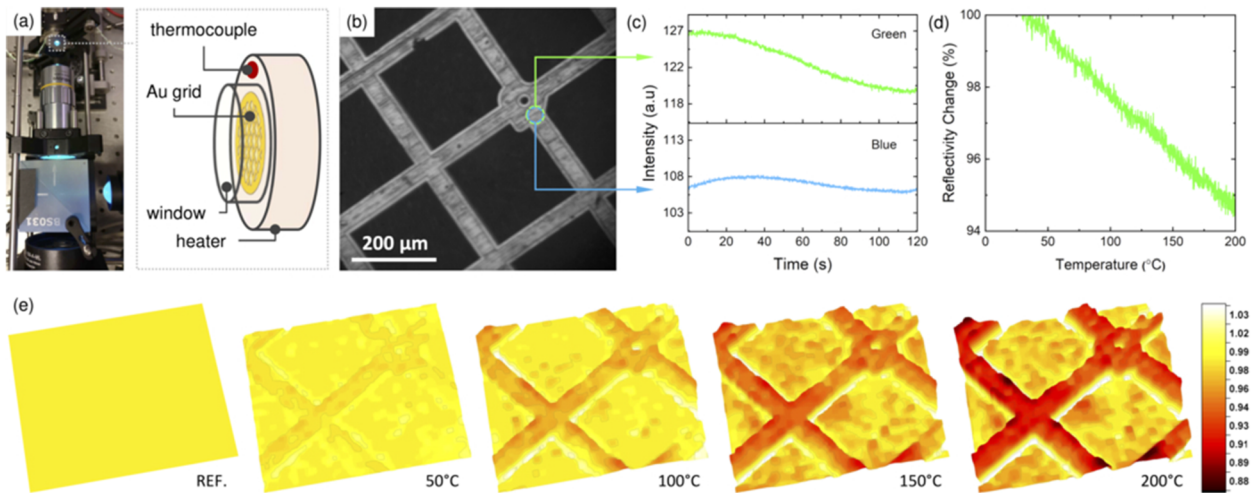


FIG. 4. (a) Experimental setup and schematic of the specimen; (b) area of the specimen visualized by the camera; (c) average pixel intensities in the area of interest (gold grid) in each color channel plotted with respect to time; (d) reflectivity change as a function of temperature measured with thermocouples; and (e) spatial profile of reflectivity change as a function of temperature.

specimen was neither permanently fixed to the glass window, nor to the heater, some movement of the specimen and change in the pixel intensity in the blue channel was also observed. This dynamic change during the test was taken into account in the temperature profile of reflectivity change, which is shown in Fig. 4(d). Finally, the spatial profile of reflectivity change as a function of temperature is shown in Fig. 4(e). The observed changes in reflectivity of the gold grid are perceptible and more pronounced with increasing temperature.

V. GOLD MODEL

The experimental observations of the temperature-dependent reflectivity of gold can be used to validate a predictive model for the reflectivity changes of the material of interest in different thermal states. In recent years, several models and approaches have been developed to simulate the optical properties of gold.^{24–30} In general, the more realistic the model, the larger number of unphysical parameters. Here, the intention was to use a model which is less demanding but at the same time captures the essential physics

involved in these phenomena. In this regard, the chosen approach is as follows:

The optical response of gold to the disturbances caused by electromagnetic radiation, such as visible light, can be defined by the complex dielectric function, $\tilde{\epsilon}$, as follows:

$$\tilde{\epsilon} = \epsilon_1 + i\epsilon_2, \quad (6)$$

where ϵ_1 and ϵ_2 are the real and imaginary part of the dielectric constant.

The contribution from the intraband transitions of bound electrons (i.e., free electrons) to the dielectric constant is described by the Drude model,

$$\epsilon_1 = \epsilon_\infty - \frac{E_p^2}{E^2 + i\gamma E}, \quad (7)$$

where E is the photon energy, E_p is the plasma energy relevant to the intraband transitions, γ is the Drude damping constant (the electron relaxation rate), and the contribution of bound electrons to the polarizability is included in ϵ_∞ (the permittivity at infinite energy).

The contribution from the interband transition of bound electrons is modeled in the simplified form of the Brendel and Bormann model³¹ proposed by Dolan *et al.*,²²

$$\begin{aligned}\varepsilon_2 &= \frac{w_B E_P^2}{2a} \ln\left(\frac{E_B + a}{E_B - a}\right), \\ a &= E^2 + i\Gamma E,\end{aligned}\quad (8)$$

where w_B , E_B , and Γ are the strength, resonance energy, and damping (broadening) factor of the oscillator for the interband transitions. This modification to the model results in a better representation of the broad absorption of light in the blue and green regions of the spectrum (which is of interest in this study). Finally, Eq. (8) assumes the following weight function:

$$w(E) = \begin{cases} 0 & \text{for } E < E_B, \\ w_B & \text{for } E \geq E_B. \end{cases} \quad (9)$$

The model has, therefore, three intraband (ε_∞ , E_P , and γ) and three interband (w_B , E_B , and Γ) parameters, which are fitted to experimental data in the visible spectrum of light by the method of least squares,

$$\chi^2 = \frac{1}{n} \sum (\tilde{\varepsilon}_{\text{experimental}} - \tilde{\varepsilon}_{\text{modeled}})^2. \quad (10)$$

Next, consider the complex index of refraction, \tilde{n} , that is related to the dielectric function, $\tilde{\varepsilon}$, as follows:

$$\begin{aligned}\tilde{\varepsilon} &= \tilde{n}^2, \\ \varepsilon_1 &= n^2 - k^2, \\ \varepsilon_2 &= 2nk,\end{aligned}\quad (11)$$

where n (refractive index) and k (extinction coefficient) are the real and imaginary parts of the complex refractive index ($\tilde{n} = n + ik$). This allows for the calculation of the reflectivity of gold for normal incidence of light as follows:

$$R = \frac{(n-1)^2 + k^2}{(n+1)^2 + k^2}. \quad (12)$$

Finally, the reflectivity response can greatly be affected by changes in temperature. These are modeled such that all six model parameters (ε_∞ , E_P , γ , w_B , E_B , and Γ) are temperature dependent in the following manner:

$$\begin{aligned}\frac{\partial \varepsilon_\infty}{\partial \mathcal{T}} &= p_1(\text{K}), & \frac{\partial E_P}{\partial \mathcal{T}} &= p_2(\text{meV/K}), \\ \frac{\partial \gamma}{\partial \mathcal{T}} &= p_3(\text{meV/K}), & \frac{\partial w_B}{\partial \mathcal{T}} &= p_4(\text{K}), \\ \frac{\partial E_B}{\partial \mathcal{T}} &= p_5(\text{meV/K}), & \frac{\partial \Gamma}{\partial \mathcal{T}} &= p_6(\text{meV/K}),\end{aligned}\quad (13)$$

where \mathcal{T} is the temperature and p_i are the coefficients obtained from the best approximation between the measured and modeled

responses in the least squared error method sense [Eq. (10)] with the following constraints:

$$\begin{aligned}\frac{\partial \Delta R(\lambda_{405})}{\partial \mathcal{T}} &\simeq 0, \\ \frac{\partial \Delta R(\lambda_{500})}{\partial \mathcal{T}} &\simeq 0, \\ \frac{\partial \Delta R(\lambda_{480})}{\partial \mathcal{T}} + \frac{\partial \Delta R(\lambda_{532})}{\partial \mathcal{T}} &\simeq 0,\end{aligned}\quad (14)$$

where $\Delta R(\lambda_i)$ is the change in reflectance at discrete wavelength, i .

The constraints are based on the experimental observations of gold reflectivity,^{12,18,19,22,32} where: (i) for ~ 405 nm wavelength the corresponding change in reflectivity is less than 1% up to 500°C , (ii) reflectance changes occur on either side of ~ 500 nm, (iii) there is a positive change in reflectance ~ 480 nm peak and negative ~ 532 nm peak, and (iv) relative change in reflectance ~ 480 nm peak is similar or equal to ~ 532 nm peak.

VI. DISCUSSION

Figure 5(a) shows a comparison between the experimental reflectivity of gold³³ and model prediction. The best-fit value of model parameters and coefficients are listed in Table I. Note that the model is not able to provide a good approximation in the red end of the spectrum, and this may be linked to the small number of data points in this part of the spectrum. Another limitation of this model is that it is not able to represent the interband transition at ~ 470 nm. While the modeling of this transition is not critical in the proposed methodology (using wavelengths out of this range), this could be taken into account by adding simple Lorentz oscillators to a Drude term. In this scenario, one should expect more model parameters that have no direct physical meaning.²⁶ The figure also shows the temperature-modulated reflectance, as can be predicted by the model. This temperature dependence of the model is also visualized in the form of reflectivity change in response to increasing temperature, where the reference measurements are taken at room temperature [Fig. 5(b)]. These model predictions are consistent with optical measurements of gold at different temperatures reported elsewhere.^{18,22} That is, the model is able to capture the temperature insensitivity at 405 and 500 nm, as well as the positive and negative change in reflectance at 480 and 532 nm, respectively. Furthermore, the model predictions for the wavelengths of interest are in good agreement with the experimental data. For example, Dolan *et al.* showed that the reflectance ratio for the unannealed and annealed gold sample at a wavelength of 532 nm and the temperature rise to 275°C is 93.5% and 93%, respectively.²² In Beran, the reflectance ratio for the same wavelength was measured to be $\sim 93.5\%$ at 300°C .¹⁸ In the present study, the model predicts the reflectance ratio to be close to 92% at the same wavelength and temperature.

Figure 6 shows a comparison between the experimental data and the model predictions for two investigated materials. In both cases, the reflectivity changes as a function of temperature in the spectrum of light associated with the green channel were well captured by the model. The error bars represent lower and upper bounds for the reflectivity changes assuming uncertainties for the model parameters. At this point, it is also worth noting the differences in the reflectivity changes between the two materials

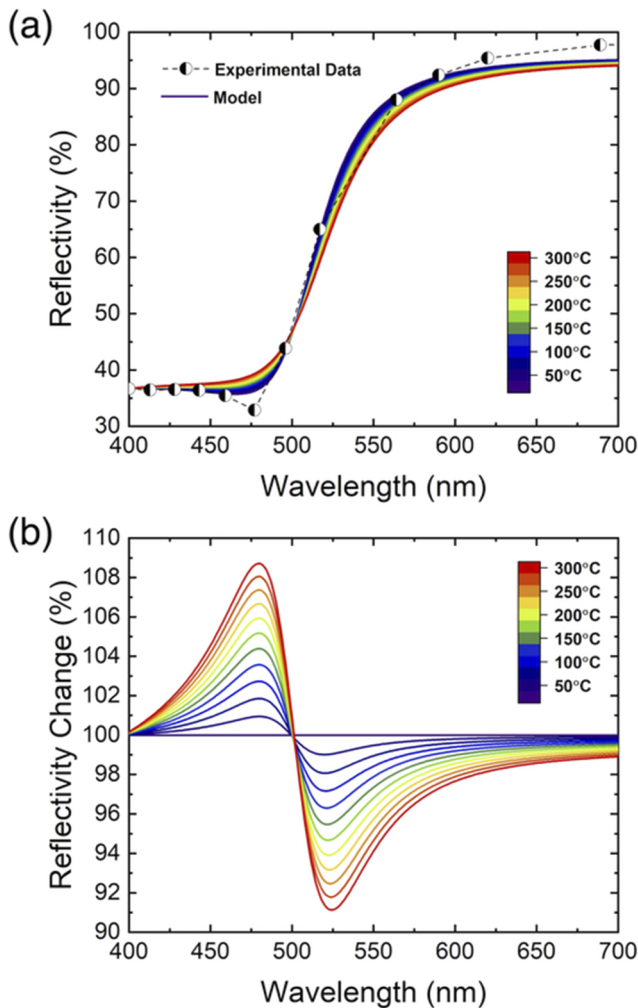


FIG. 5. (a) Reflectance and (b) reflectance ratio predictions for gold between room temperature and 300 °C.

(~0.5% at 200 °C). Here, the gold film can be considered as an ideal case for the reflectivity measurements, where the material is deposited on a flat surface and not exposed to air. In general, the electrodeposition process results in fine-grained thin films, and

one can expect the enhanced electron collisions associated with the micro-/nano-scale surface texturing and high density of grain boundaries when conducting the reflectivity measurements.³⁴ Also, the gold film was supported by a glass surface that limited its thermal movement and kept in the focus plane during the test. The gold grid was not prevented from such movement, and this increased the possibility of light leakage between the adjacent pixels/regions. In addition, the reflectivity measurements of the gold grid could be affected by the bulk character of the specimen, porosity, and/or surface contamination.^{34–37} The authors acknowledge these effects, which in the present study are difficult to quantify. With that in mind, the interpretation of the model parameters and coefficients that shows the same trends for both materials is as follows:

- (i) The values of all six parameters are resulting from the best mathematical solution to the problem, the given model, the experimental data, and the fit to the visible spectrum of light. Different data or electromagnetic ranges would likely provide a different solution.
- (ii) The change of ϵ_∞ with increasing temperature is insignificant, and difficult to ascribe to any known mechanism. Similar conclusions have been drawn from other studies.^{22,30}
- (iii) The square of the plasma frequency (E_p) is proportional to the electron density and inversely proportional to the electron effective mass. Both play a role in the temperature dependency of E_p , which is explained by the two counteracting mechanisms. In the first case, the electron density can be reduced by increasing temperature (caused by thermal expansion), and this consequently reduces E_p . The second mechanism links the increasing E_p to the fact that the effective mass in metals can decrease with increasing temperature.^{30,38} The observed positive change in E_p with increasing temperature suggests that the electron effective mass decreases faster than the electron density. This trend was also reported by Dolan *et al.*²²
- (iv) thermal vibrations of the atoms increase with increasing temperature, and so too does the number of released photons. The temperature dependence of γ is determined by the scattering mechanism (mainly by the electron–phonon scattering for a bulk sample). Thus, the higher the temperature, the higher the γ value.^{22,30}
- (v) There is no change in w_B in the investigated temperature range. A similar observation has been reported elsewhere.²²
- (vi) The shift of the interband absorption ~2.5 eV decreases progressively with temperature,^{17,39,40} and this feature of the

TABLE I. Model parameters and coefficients.

	Value	Gold film coefficients, p_i	Gold grid coefficients, p_i
ϵ_∞	1.03 ± 0.005	$602.5 \pm 0.5 \times 10^{-6} \text{ (}^\circ\text{C)}$	$555.0 \pm 0.5 \times 10^{-6} \text{ (}^\circ\text{C)}$
E_p	$11.81 \pm 0.005 \text{ (eV)}$	$0.0478 \pm 0.0005 \text{ (meV/}^\circ\text{C)}$	$0.0269 \pm 0.0005 \text{ (meV/}^\circ\text{C)}$
γ	$0.27 \pm 0.005 \text{ (eV)}$	$0.177 \pm 0.0005 \text{ (meV/}^\circ\text{C)}$	$0.108 \pm 0.0005 \text{ (meV/}^\circ\text{C)}$
w_B	0.16 ± 0.005	$-1 \pm 0.5 \times 10^{-8} \text{ (}^\circ\text{C)}$	$-1 \pm 0.5 \times 10^{-8} \text{ (}^\circ\text{C)}$
E_B	$2.51 \pm 0.005 \text{ (eV)}$	$-0.085 \pm 0.0005 \text{ (meV/}^\circ\text{C)}$	$-0.102 \pm 0.0005 \text{ (meV/}^\circ\text{C)}$
Γ	$0.29 \pm 0.005 \text{ (eV)}$	$0.375 \pm 0.0005 \text{ (meV/}^\circ\text{C)}$	$0.289 \pm 0.0005 \text{ (meV/}^\circ\text{C)}$

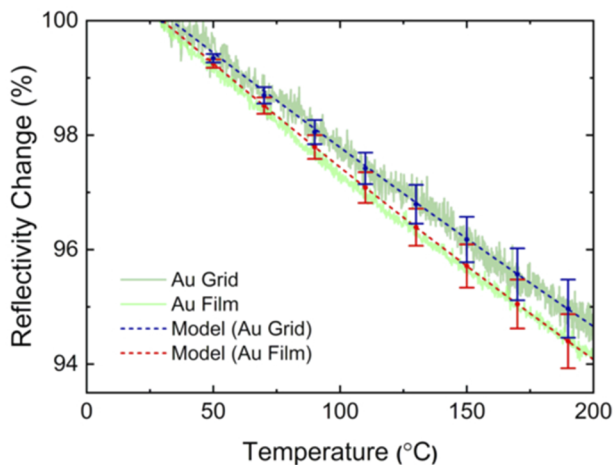


FIG. 6. Comparison between the experimental data and the model predictions. The error bars stem from the uncertainties associated with the model parameters.

absorption edge was captured well by the model (E_B decreases with temperature).

- (vii) Γ is of the same order of magnitude as γ and increases at almost the same rate with increasing temperature. Dolan *et al.* reported the same relative change of the two factors, but their values differ by one order of magnitude.²²

VII. SUMMARY

The proposed experimental approach has been shown to be valid for a single point measurement of reflectivity by averaging the light intensity over a region of interest. In that case, the spot size of any given measurement is largely controlled by the microscope objective located in front of the specimen. However, one of the main characteristics of this apparatus is that it is suitable for spatial reflectance measurements, where two probing signals can be simultaneously captured by a single camera. This creates an opportunity for temperature measurements of the fast-changing phenomenon using state-of-the-art high-speed cameras. For example, this technique can be used to determine temperature fields in the test specimens undergoing dynamic shear deformation, which results in strain localization causing adiabatic shear band formation over tens of nanoseconds. This mechanism will be explored with this apparatus in our future studies. The analytic model was able to predict the complex dielectric function of gold in the range of visible light. The temperature dependence of model parameters was found to be consistent with the literature and explained by the physical principles governing the behavior of gold at elevated temperatures.

ACKNOWLEDGMENTS

This research was supported by the UK Engineering and Physical Sciences Research Council (EPSRC) grant, “Heterogeneous Mechanics in Hexagonal Alloys across Length and Time Scales”

(Grant No. EP/K034332/1). The authors also gratefully acknowledge the financial support from the Air Force Office of Scientific Research (AFOSR) and the Georgia Institute of Technology (Grant No. FA9550-15-1-0499). The authors are grateful to David Chapman (University of Oxford) for valuable discussions during the progress of this work.

AUTHOR DECLARATIONS

Conflict of Interest

The authors have no conflicts to disclose.

Author Contributions

L. Farbaniec: Data curation (equal); Formal analysis (lead); Investigation (lead); Methodology (equal); Project administration (equal); Writing – original draft (lead); Writing – review & editing (equal).
D. E. Eakins: Conceptualization (lead); Data curation (equal); Funding acquisition (lead); Methodology (equal); Project administration (equal); Supervision (lead); Writing – review & editing (equal).

DATA AVAILABILITY

The data that support the findings of this study are available from the corresponding authors upon reasonable request.

REFERENCES

- ¹X. Maldague, *Theory and Practice of Infrared Technology for Nondestructive Testing* (John Wiley & Son, 2001).
- ²M. F. Modest, *Radiative Heat Transfer* (Academic Press, 2013).
- ³R. Rosei and D. W. Lynch, *Phys. Rev. B* **5**, 3883 (1972).
- ⁴G. L. Eesley, *Phys. Rev. Lett.* **51**, 2140 (1983).
- ⁵C. A. Paddock and G. L. Eesley, *J. Appl. Phys.* **60**, 285 (1986).
- ⁶K. Maize, D. Kendig, A. Shakouri, and V. Vashchenko, in *2011 International Reliability Physics Symposium* (IEEE, 2011), p. EL-4.
- ⁷K. Maize, G. Pavlidis, E. Heller, L. Yates, D. Kendig, S. Graham, and A. Shakouri, in *2014 IEEE Compound Semiconductor Integrated Circuit Symposium (CSICS)* (IEEE, 2014), pp. 1–8.
- ⁸W. Si, L. Zheng, and S. Wei, in *2019 20th International Conference on Electronic Packaging Technology (ICEPT)* (IEEE, 2019), pp. 1–4.
- ⁹S. Alajlouni, K. Maize, P. Bermel, and A. Shakouri, in *ASME 2019 International Technical Conference and Exhibition on Packaging and Integration of Electronic and Photonic Microsystems* (American Society of Mechanical Engineers Digital Collection, 2019).
- ¹⁰D. Wang, Z. Liu, L. Zheng, and W. Liu, in *2019 20th International Conference on Electronic Packaging Technology (ICEPT)* (IEEE, 2019), pp. 1–5.
- ¹¹T. Zhu, D. Olson, P. Hopkins, and M. Zebajadi, *Rev. Sci. Instrum.* **91**, 113701 (2020).
- ¹²G. Tessier, S. Holé, and D. Fournier, *Appl. Phys. Lett.* **78**, 2267 (2001).
- ¹³M. Farzaneh, K. Maize, D. Luerßen, J. A. Summers, P. M. Mayer, P. E. Raad, K. P. Pipe, A. Shakouri, R. J. Ram, and J. A. Hudgings, *J. Phys. D: Appl. Phys.* **42**, 143001 (2009).
- ¹⁴B. Vermeersch, J. Christofferson, K. Maize, A. Shakouri, and G. De Mey, in *2010 26th Annual IEEE Semiconductor Thermal Measurement and Management Symposium (SEMI-THERM)* (IEEE, 2010), pp. 228–234.
- ¹⁵J. Yang, C. Maragliano, and A. J. Schmidt, *Rev. Sci. Instrum.* **84**, 104904 (2013).
- ¹⁶T. Favalaro, J. Suh, B. Vermeersch, K. Liu, Y. Gu, L.-Q. Chen, K. X. Wang, J. Wu, and A. Shakouri, *Nano Lett.* **14**, 2394 (2014).

- ¹⁷P. Winsemius, F. F. van Kampen, H. P. Lengkeek, and C. G. v. Went, *J. Phys. F: Met. Phys.* **6**, 1583 (1976).
- ¹⁸A. Beran, *Tschermaks Mineral. Petrogr. Mitt.* **34**, 211 (1985).
- ¹⁹M. G. Burzo, P. L. Komarov, and P. E. Raad, in *Twenty-Second Annual IEEE Semiconductor Thermal Measurement and Management Symposium* (IEEE, 2006), pp. 87–94.
- ²⁰C. Cardenas, D. Fabris, S. Tokairin, F. Madriz, and C. Y. Yang, *J. Heat Transfer* **134**, 111401 (2012).
- ²¹T. Favaloro, J.-H. Bahk, and A. Shakouri, *Rev. Sci. Instrum.* **86**, 024903 (2015).
- ²²D. H. Dolan, C. T. Seagle, and T. Ao, SANDIA Report No. SAND2013-8203, 2013.
- ²³T. G. White, J. R. W. Patten, K.-H. Wan, A. D. Pullen, D. J. Chapman, and D. E. Eakins, *Strain* **53**, e12226 (2017).
- ²⁴A. D. Rakić, A. B. Djurišić, J. M. Elazar, and M. L. Majewski, *Appl. Opt.* **37**, 5271 (1998).
- ²⁵A. Vial, A.-S. Grimault, D. Macías, D. Barchiesi, and M. L. De La Chapelle, *Phys. Rev. B* **71**, 085416 (2005).
- ²⁶P. G. Etchegoin, E. C. Le Ru, and M. Meyer, *J. Chem. Phys.* **125**, 164705 (2006).
- ²⁷T. Brandt, M. Hövel, B. Gompf, and M. Dressel, *Phys. Rev. B* **78**, 205409 (2008).
- ²⁸R. L. Olmon, B. Slovick, T. W. Johnson, D. Shelton, S.-H. Oh, G. D. Boreman, and M. B. Raschke, *Phys. Rev. B* **86**, 235147 (2012).
- ²⁹D. Rioux, S. Vallières, S. Besner, P. Muñoz, E. Mazur, and M. Meunier, *Adv. Opt. Mater.* **2**, 176 (2014).
- ³⁰H. Reddy, U. Guler, A. V. Kildishev, A. Boltasseva, and V. M. Shalae, *Opt. Mater. Express* **6**, 2776 (2016).
- ³¹R. Brendel and D. Bormann, *J. Appl. Phys.* **71**, 1 (1992).
- ³²D. H. Dolan, T. Ao, and C. T. Seagle, *AIP Conf. Proc.* **1552**(1), 767–770 (2013).
- ³³M. J. Weber, *Handbook of Optical Materials* (CRC Press, 2002), Vol. 19.
- ³⁴M.-L. Thèye, *Phys. Rev. B* **2**, 3060 (1970).
- ³⁵P. B. Johnson and R. W. Christy, *Phys. Rev. B* **6**, 4370 (1972).
- ³⁶D. E. Aspnes, E. Kinsbron, and D. D. Bacon, *Phys. Rev. B* **21**, 3290 (1980).
- ³⁷V. Svetovoy, P. Van Zwol, G. Palasantzas, and J. T. M. De Hosson, *Phys. Rev. B* **77**, 035439 (2008).
- ³⁸C.-Y. Young, *J. Phys. Chem. Solids* **30**, 2765 (1969).
- ³⁹W. J. Scouler, *Phys. Rev. Lett.* **18**, 445 (1967).
- ⁴⁰P. Winsemius, M. Guerrisi, and R. Rosei, *Phys. Rev. B* **12**, 4570 (1975).